Effect of varying carbon microstructures on the ion storage behavior of dual carbon lithium-ion capacitor

Udita Bhattacharjee, Abhay Gautam, Surendra K. Martha [*]

Department of Chemistry, Indian Institute of Technology Hyderabad, Kandi, Sangareddy, Telangana 502284, India

ARTICLE INFO

ABSTRACT

Dual carbon lithium-ion capacitors (LICs) are the next-generation hybrid energy storage devices that aim towards energy-power balanced applications. Thus, tuning the properties of the carbon electrode materials is a crucial step toward optimizing the device's performance. Herein, the effect of change in the microstructure of the carbon electrodes on the ion storage capacity and their consequent energy-power manifestation is investigated. The optimized carbonaceous anode calcined at 700 ºC delivers 290 mAh g^{-1} capacity after 1000 cycles at 1 A g^{-1}. This superiority in performance is attributed to the formation of micron-size channels and mesopores for better ion transport and storage. In contrast, the activated carbon cathode delivers a capacitance of 118 F g^{-1} and retains 76% at the end of 5000 cycles. The LIC full cell with these electrode materials provides maximum energy of 120 Wh kg^{-1}, a maximum power density of 20.7 kW kg^{-1} and cycles till 9000 cycles with ~67% capacitance retention. The mechanistic control over the deliverable ion storage capacity is also analyzed for the LIC full cell. Furthermore, the lighting demonstration, self-discharge studies, leakage current, and electrochemical impedance are recorded to elucidate the practical feasibility and performance degradation mechanism of the coin-cell device.

1. Introduction

Lithium-ion capacitors (LICs) are hybrid devices that blend the characteristics of high-energy lithium-ion batteries (LIBs) and high-power supercapacitors into a single-unit device. These devices aim to have a balanced performance matrix in the intersection of widely researched and successful electrochemical energy storage devices like lithium-ion batteries and supercapacitors. LICs are usually assembled with one lithium-ion battery-type electrode (intercalation-type carbonaceous, intercalation and conversion-type metal oxides, and alloy-type anodes, metal oxide and phosphate cathode) and one electric double layer type electrode (usually activated carbon) in a non-aqueous electrolyte containing Li-salt like the conventional LIB electrolyte, i.e., 1 M $LiPF_6$ in a mixture of carbonate solvents [1–5]. The first LIC was studied using lithium titanate and activated carbon by Amatucci et al. and in the recent years LICs with pre-lithiated graphite, disordered carbon or lithium titanate LIB-type electrode and electric double layer capacitor (EDLC)-type activated carbon are being commercialized worldwide [6]. However, certain roadblocks persist in achieving the optimal performance due to the difficulty in balancing the kinetics of the slower LIB-type electrode and the faster EDLC-type electrode. As a result, the conventional capacity and mass balancing strategies may not be of utility. The balancing strategy becomes unique for each system depending on the charge acceptance capability at different current rates for each type of electrode. Thus, in line with this issue of LICs, dual carbon configurations using one LIB-type disordered carbon with high-rate capability and EDLC-type activated carbon is found to be suitable for LIC development [7].

The mechanism involved for the ion storage in an LIC is different for both the electrodes. For conventional LICs, during charge, the Li^+ from the electrolyte salt intercalates in the LIB-type anode and PF_6^- gets adsorbed on the surface of the EDLC-type electrode. But this mechanism results in irreversible trapping of Li-ions in the LIB anode due to secondary reactions on the electrode-electrolyte interface. Thus, pre-lithiated LIB-type anode, LIB-cathode, or hybrid LIB-AC cathode with additional Li-replenishment sources have been researched in order to increase the cycle life as well as the energy output of LICs. The configuration with pre-lithiated LIB anode and AC cathode is found to be optimal as this introduces a parallel additional mechanism during charge storage along with solving the problem of degrading cycle life

performance. Above the open circuit voltage (OCV) of the LIC cell, charge storage mechanism is similar to that of the conventional LICs where during charging Li^+ from the electrolyte intercalates into the LIB-type anode and PF_6^- gets adsorbed on the cathode surface and vice versa on charging. But below OCV, during discharge the pre-lithiated Li^+ from the anode diffuses out and gets adsorbed on the activated carbon cathode surface which is reversed during charging [8–10]. Thus, LICs with this configuration can achieve higher energy densities and longer cycle life which have led them to the path of commercialization.

Disordered carbons from various inexpensive and bio-waste sources as LIB-type anodes for LICs have been of interest because of their better high current rate capability, raw material availability, and feasible extraction routes compared to ordered carbon. This property arises due to the multiple charge storage mechanisms of different kinetics taking place in case of Li-ion storage in disordered carbon. The series of mechanisms which contribute towards the Li-ion storage include adsorption (chemisorption on the heteroatom functionalities and physical adsorption on the edges of disordered sheets), intercalation in the inter-layer spaces, and nano-micropore filling [11,12]. But the open carbon network edges, presence of ultra-micropores and hetero-functional groups also result in high irreversible capacity during initial cycles due to more secondary reactivity with electrolyte. Minimizing the initial irreversible capacity is also an important aspect for practical usability of disordered carbons. Thus, disordered carbon matrix provide space for Li-ions depending on their morphology and micro/nano-structuring as the Li-ion storage is not site limited. Pre-treatment of raw materials and calcination temperatures can be the controlling factors in the physical characteristics and subsequent Li-ion storage of disordered carbon. Thus, tuning the physical properties of the disordered carbon may be the way towards enhancing the optimal Li-ion storage.

Activated carbon is the most widely used EDLC-type cathode in LICs, which utilizes the adsorption-desorption phenomenon to store ions on the surface. Thus, surface properties like high surface area, combination of micro and meso porosity, and presence of hetero functional groups of the activated carbon are the most important aspects that govern the Li-ion storage performance. The desired surface area for optimum performance of activated carbon is >1000 m^2g^{-1}. Also, an optimum blend of micro (~ 2 nm) and *meso* (2–50 nm) pores is desired for proper functioning in an LIC as micropores provide the space for adsorption and mesopores facilitate the channel in order to access the micropores [13–16]. But the ultra-micropores <0.5 nm in size can result in irreversible trapping of the ions and performance degradation. Further, the presence of hetero functional groups explores the scope for ion-storage through chemisorption [17,18]. Thus, balancing the properties for optimum charge storage is of utmost importance.

Dual carbon LICs assembled with disordered carbon and activated carbon derived from waste sources have been widely studied by researchers due to their abundance, feasibility, uniqueness in terms of morphology and physical characteristics dependent on the raw material and extraction method used and better deliverable performances [19–23]. The LIC devices with configurations of (Anode// cathode) olive pit//activated olive pit, sisal fiber derived carbon// sisal fiber derived activated carbon, defect rich nitrogen-doped carbon from sepia biowaste// polyimide microsphere derived activated carbon, graphene-coffee waste-derived carbon// activated carbon, CNT-phenol functionalized melamine derived carbon//CNT, asphalt-derived carbon//asphalt-derived carbon, and order-disorder carbon//activated carbon delivers energies of 100, 104, 101.7, 100, 111.8, 120 and 112 Wh kg^{-1} at power densities of 150. 143, 250, 9000, 325, 850, and 260 W kg^{-1}, respectively [24–30].

Herein, we have fabricated a LIC using mechanistically different carbons derived from one of the most common agro-waste, i.e., onion peel. Onion peel was chosen as the raw material of choice as it is inexpensive waste, easily available worldwide, and contains flavonoids, vitamins, and minerals in addition to carbohydrates, which may result in

the derivation of hetero-atom functionalization of the carbon matrix formed [31–33]. The raw materials were pretreated chemically in a different manner using the same hydrothermal synthesis technique followed by calcination at different temperatures. This resulted in the development of carbon matrices with different microstructures and ion storage properties. This dependence of the Li-ion storage efficiency on the varying microstructure is studied. Finally, LICs are assembled using the optimal Li-storing battery-type carbon and the as-synthesized activated carbon. The performance matrix of the dual carbon LIC was analyzed through their balanced energy-power output, cycle life, and feasibility studies like self-discharge, leakage current, and electrochemical impedance spectra during prolonged cycling.

2. Experimental section

2.1. Synthesis of agro-waste derived anode material (AWAx where x corresponds to the calcination temperature i.e., 6,7,8 for 600, 700, and 800 °C, respectively) and agro-waste derived activated carbon (AWAC)

The agro-waste onion peel was collected in bulk from agricultural wasteland, washed thoroughly to remove any dirt trace, and dried overnight in a hot air oven. The dried mass was then grinded into powder. For the synthesis of LIB-type anode active material, it was mixed with thiourea (as a source of additional N and S) in 1:3 ratio and put in hydrothermal at 200 °C for 15 h. The resultant was dried overnight in a hot air oven and calcined in inert atmosphere at 600, 700, 800 °C for 2 h to obtain AWA6, AWA7, and AWA8, respectively, after subsequent washing and drying. For the synthesis of the capacitive cathode material, the dried mass was mixed with KOH in 1:3 ratio for activation and calcined at 800 °C for 2 h to induce porosity and consequent high surface area through the series of chemical reaction taking place as explained in Supplementary Material [14]. A schematic representation of the synthesis procedure is provided in the Scheme 1. All physical, structural, and electrochemical characterizations were carried out at room temperature, i.e., 25 °C.

2.2. Physical and structural characterization

The synthesized carbon matrices were structurally characterized using X-ray diffraction (XRD) with an X-ray diffractometer (Bruker Inc., Germany) which utilizes Cu-k$_\alpha$ radiation and θ-θ geometry. Raman spectroscopy for the samples was analyzed using a Witec alpha300 Raman spectrometer by a laser beam of 532 nm in the range of 400-3000 cm^{-1}. Fourier transform infrared spectroscopy (Bruker Alpha-P FTIR spectrometer) in the range 500–4000 cm^{-1} and X-ray photoelectron spectroscopy (Axis Supra, Kratos Analytical Pvt. Ltd.) using Al k$_\alpha$ and calibrated with C1s =284.3 eV were used to analyze the bonding characteristic between neighboring atoms and the quantifiable presence of hetero atoms. The morphology of the samples was studied using transmission electron microscopy (Jeol JEM F200) and scanning electron microscopy (Jeol JIB 4700F). The surface area, porosity distribution, and size were analyzed using a BET analyzer (Micromeritics ASAP 2020), and the degassing was performed at 200 °C for 4 h.

2.3. Electrode fabrication and cell assembly

A slurry was prepared using 80 wt.% electrode active material, 10 wt.% conductive carbon additive (Super P-C65), 10 wt.% polyvinyl difluoride binder (Kureha 1700) in N-methyl pyrrolidone solvent (Sigma Aldrich Ltd.) and coated onto Cu-foil for the anode and carbon-coated Al-foil for the cathode. These coated foils were vacuum-dried at 70 °C overnight and roll-pressed thereafter. 10 mm diameter electrodes were punched out from the coated foils. The active mass loading for the cathode is maintained in the range of ~1.5- 2.0 mg cm^{-2}, and that of the anode was kept within ~1 mg cm^{-2}.

The anodes and cathode were individually assembled in a CR2032
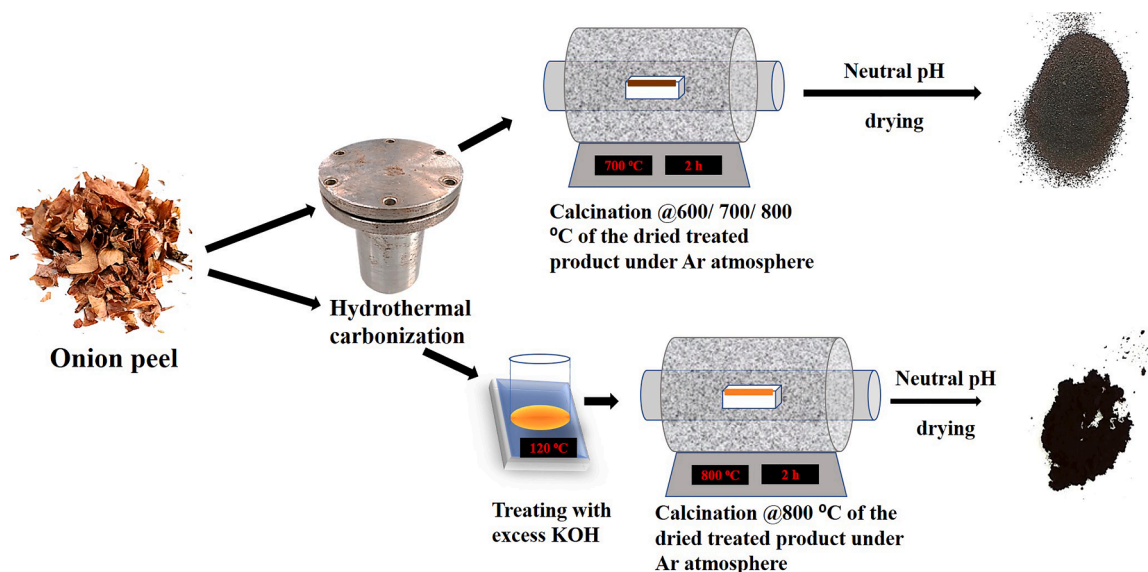
Scheme 1. A schematic representation of anode and cathode active material preparation from onion peel.

coin cell setup in a half-cell configuration with 12 mm punched Li foil as counter as well as reference electrode separated by a GF/D separator and dipped in 1 M LiPF$_6$ in EC: DEC electrolyte. Prior to full cell assembly, a mechanical pre-lithiation method is used where a calculated amount of 10 µ thick lithium chip is kept in contact with the anode with mechanical pressure [34]. The pre-lithiated anode (AWAx) is then assembled with the cathode (AWAC) in a 1:3 mass ratio with a cellulose fiber separator (for better electrolyte absorption) and the same electrolyte.

2.4. Electrochemical characterization

The electrochemical tests were performed in a 1455A series frequency response analyzers coupled cell test system-1470E multi-channel potentiostats (Solartron Analytical, USA). The anode, cathode half-cells, and LIC full-cells were characterized using cyclic voltammetry in the optimum potential range of 0.01–3.0 V, 1.5- 4.0 V, and 1.5- 4.0 V, respectively, at varying potential sweep rates (0.05 – 5 mV s^{-1} for anode half cells, 0.5 – 20 mV s^{-1} for cathode half-cells, and 0.2- 10 mV s^{-1} for full cells). The constant current charge-discharge cycles were performed at varying current densities (0.1- 5 A g^{-1} for the anode, 0.5- 10 A g^{-1} for the cathode, and 0.2- 10 A g^{-1} for the full cells). The cycling life tests were performed at 1 A g^{-1} current density.

To understand the practical feasibility and applicability of the LIC full cell, self-discharge was recorded for the cell after charging till 4 V at 1 A g^{-1}. The leakage current for the cell was recorded by holding the potential at the highest potential of operation, i.e., 4 V for 10 h. 3 LED lights connected in series were demonstrated using one LIC full cell after

charging at 1 A g^{-1} current density. Electrochemical impedance spectroscopy was recorded in the frequency range 10^6 – 10^{-2} Hz before and after cycling for the LIC full cell to understand the failure mechanism.

3. Results and discussion

XRD pattern of the anode (AWA6, AWA7, and AWA8) and cathode (AWAC) active materials (Fig. 1a) show a broad characteristic graphitic (002) peak with a maximum at 25.1 ° for AWA6, 25.8 ° for AWA7, and AWA8, and 24.1 ° for AWAC. A feeble signal at ~43 ° corresponding to the (100) plane is visible in the diffraction pattern of all the anode and cathode active materials. The increase in peak maximum from 25.1 ° to 25.8 ° when the calcination temperature of the active material is increased to 700, and 800 ºC from 600 ºC indicates a slight decrease in the interlayer distance between the sheets. Also, there is a slight decrease in the broadness of the peak in the case of anode active materials when the calcination temperature is increased, which signifies an increase in the ordered nature of the matrix with an increase in calcination temperature as reported in the literature. Moreover, AWAC, being activated carbon, shows a broad peak with a larger interlayer distance ensuring higher irregularity than the anode active materials. Raman spectra of the carbon samples further shed light on the degree of homogeneity and defect in the carbon matrices (Fig. 1b). The progression of the I_D/I_G ratio for the anode materials in the order of I_D/I_G (AWA6, 1.5) < I_D/I_G (AWA7, 1.35) < I_D/I_G (AWA8, 1.12) shows the increase in the ordered nature of the bonding in the carbon matrix with an increase in the calcination temperature although all the samples have
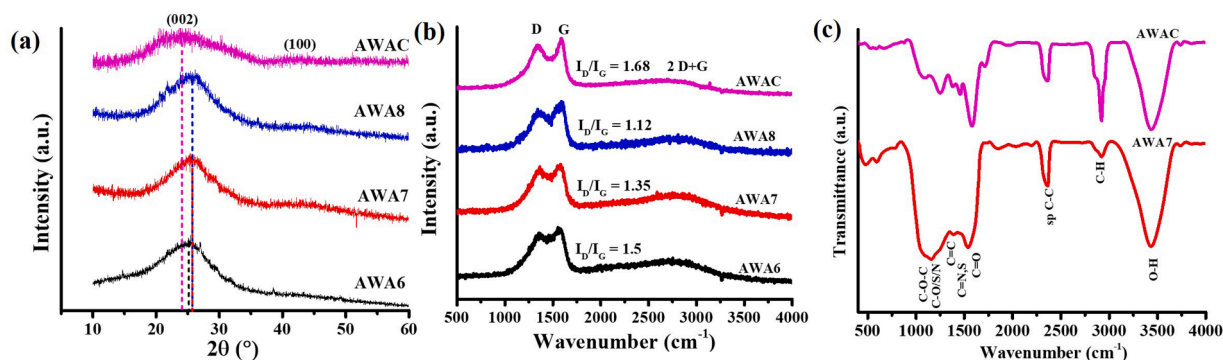

Fig. 1. (a) XRD patterns and (b) Raman spectra of AWA6, AWA7, AWA8, and AWAC. (c) FTIR spectra of AWA7 and AWAC.

$I_D/I_G > 1$ is indicating a characteristic disordered matrix. However, AWAC has the highest value of I_D/I_G (1.68), confirming the higher disordered nature of the matrix. The FTIR spectra of both AWA7 and AWAC were studied to understand the presence of heteroatom functionalities other than carbon (Fig. 1c). Both AWA7 and AWAC indicate the presence of heteroatoms, including oxygen, nitrogen, and sulfur, as peaks at frequencies corresponding to -C-O-, -C = O, -O-H, -C = S, -C = N, -C-S/N- in addition to the sp2, sp3 and sp C—C bonding frequencies. These FTIR spectra may be suggestive of the nitrogen and sulfur doping combined with oxygen functionalization of the matrix [35].

X-ray photoelectron spectra (XPS) of AWA7 and AWAC were studied to understand the elemental composition of the matrices and also the individual element bonding environment with respect to each other (Fig. 2). The survey scan for AWA7 shows the occurrence of carbon, oxygen, nitrogen, and sulfur in atomic percentages of 76%, 11.9%, 9.4%, and 2.7%, respectively. In contrast, the AWAC consists of 90.6% carbon, 7.3% oxygen, 1.6% nitrogen, and 0.6% sulfur (Supplementary Fig. S1). The low percentages of nitrogen and sulfur in the activated carbon matrix are due to the reaction with KOH during the activation process. The deconvoluted spectra for C1s in the case of AWA7 and AWAC reveal the presence of -C = C-, -C-O, -C = S, -C = O/-C = N, -O-C = O bonds in the matrix indicated by peaks at 284.3, 285.2–285.8, 286.7, 288.1, and ~291 eV, respectively. The deconvoluted O1s spectra of AWAC and AWA7 indicate the presence of -N = O, -S = O, -C-O—H, -C-O—C-, C = O, and -O-C = O bonds corresponding to the peaks at 529.2–530, 530–530.5, 531.8, 532.1–532.5, 533.3–533.5, and 534.5–534.8, respectively. Further, AWAC additionally contains adsorbed oxygen on the surface. The deconvoluted N1s spectra show peaks for the presence of aromatic pyridinic, pyrrolic, imide, graphitic, and -C-*N* = *O* bonds at 397.5–397.8, 398.2–399.1, 400.1, 401.1–401.7, 402.8–403 eV, respectively. Additionally, the deconvoluted S2p spectra of AWAC indicate the presence of -S-C-, -S-O, -*S* = *O*, -SO₂, and -SO₃ bonds corresponding to peaks at 163.1, 164.6–164.8, 167.3, 168, 168.8 eV, respectively. The deconvoluted peaks for individual elements are in accordance with each other and justify the suggestive bonding environment and hetero atom (N, S) doping [36,37].

The SEM images of AWA6 (Fig. 3a), AWA7 (Fig. 3b), and AWA8 (Fig. 3c) were studied to understand the morphological changes due to the pretreatment and calcination temperatures. All these samples show primary sheet-like features, which are supposedly a result of the retention of the inherent microstructure of the raw material under the hydrothermal condition. But the change in calcination temperature results

in the change of secondary microstructures. AWA6 (Fig. 3a) shows sheets-like structures agglomerated to form irregular shapes. In comparison, AWA7 (Fig. 3b) shows the formation of channels of micro-sized width through the folding of sheets to allow comparatively more efficient passage for the Li-ions and better accessibility to the active sites. However, when the calcination temperature is further increased to 800 ºC, the AWA8 (Fig. 3c) shows the breakage of the sheet like structure disrupting the micro sized channels formed at 700 ºC. The SEM images of AWAC (Fig. 3d) shows disorderedly arranged particles of irregular shape and size. The TEM images of AWA6 (Fig. 3e), AWA7 (Fig. 3f), and AWA8 (Fig. 3g) further confirms their sheet like primary structures. Moreover, AWA7 reveals the presence of 50 nm or lesser diameter channels formed by the sheets in addition to the micro-sized channels revealed by SEM image (Fig. 3b). These nanochannels are not prominent in case of the AWA6 samples (Fig. 3e) and in the case of AWA8 (Fig. 3g) these channels appear to be disrupted by fragmented sheets. In contrast, the TEM image of AWAC appears to be irregular shapes formed as a result of fragmentation of the sheet-like structure during the activation process.

The as-synthesized carbonaceous active materials (AWA6, AWA7, AWA8, and AWAC) were analyzed through N_2 adsorption and desorption studies to understand the surface area, particle size, pore size, and distribution of the samples to understand their feasibility of performing as either anode or cathode for lithium-ion capacitors. The N_2 adsorption and desorption isotherm for all the samples were found to follow a type IV(a) isotherm with an H4 hysteresis loop (Fig. 4a,b). This kind of isotherm is a characteristic of micro-mesoporous matrix in accordance with the IUPAC standards [38]. The considerable uptake of N_2 at low partial pressure in the case of AWAC is suggestive of the presence of a higher amount of micropores in the matrix. The BET surface areas of AWA6, AWA7, AWA8, and AWAC were found to be 1.5, 3, 12, and 1051 m² g⁻¹, respectively. Further, the Barrett-Joyner-Halenda (BJH) and DFT pore size distribution plot shows a blend of differently sized pores for all the samples with an average pore size of 29.1, 16.7, 8.6, and 3.6 nm for AWA6, AWA7, AWA8, and AWAC, respectively with an average pore volume density of 0.0041, 0.0097, 0.017, 0.554 cm³ g⁻¹. Thus, the higher surface area, microporosity with a balanced amount of mesoporosity, a higher pore volume density (Fig. 4b,d), and hetero surface functionalities (Figs. 1c, 2e–g) of AWAC makes it a justifiable choice for the capacitive electrode for the lithium-ion capacitor. In comparison, the plausible anode active materials show lower surface area. When the calcination temperature was 600 ºC, there was no proper pore formation, as seen in Fig. 4c. But when the temperature is increased to 700 ºC,
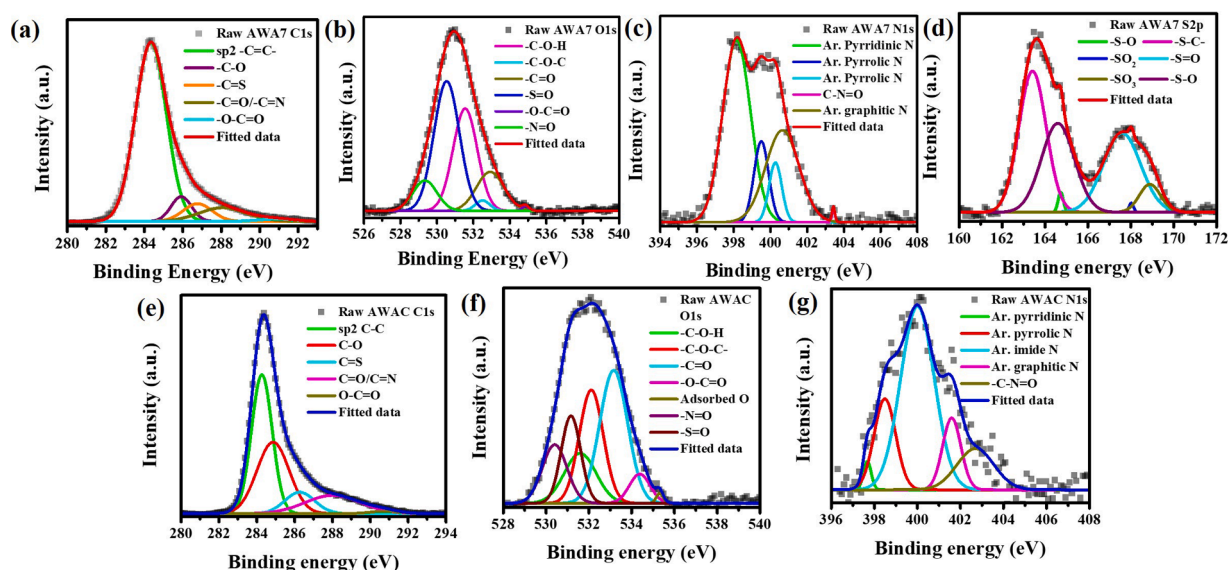

Fig. 2. Deconvoluted XPS of AWA7 (a) C1s, (b) O1s, (c) N1s, and (d) S2p. Deconvoluted XPS of AWAC (e) C1s, (f) O1s, and (g) N1s.
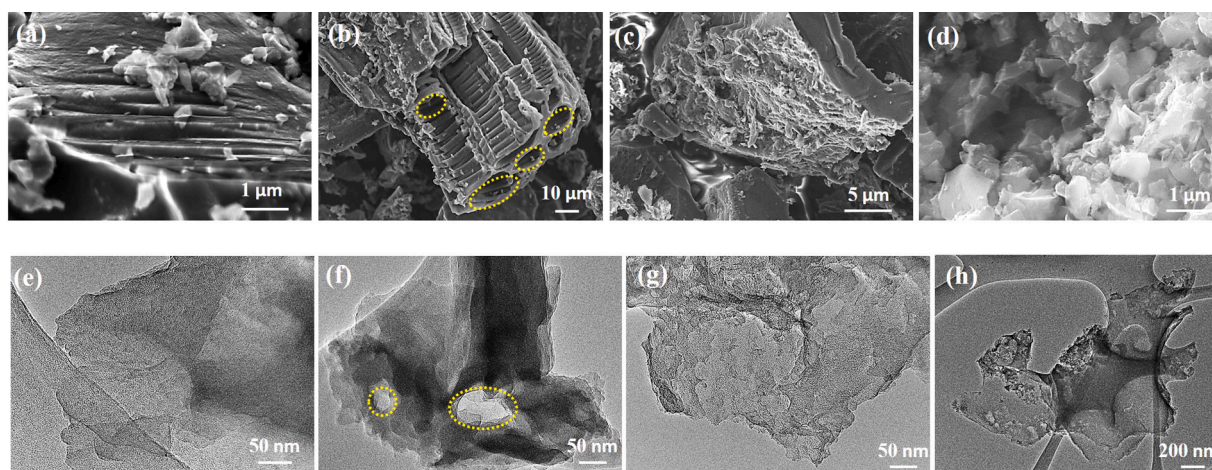
Fig. 3. SEM images of (a) AWA6, (b) AWA7, (c) AWA8, and (d) AWAC. TEM images of (a) AWA6, (b) AWA7, (c) AWA8, and (d) AWAC.
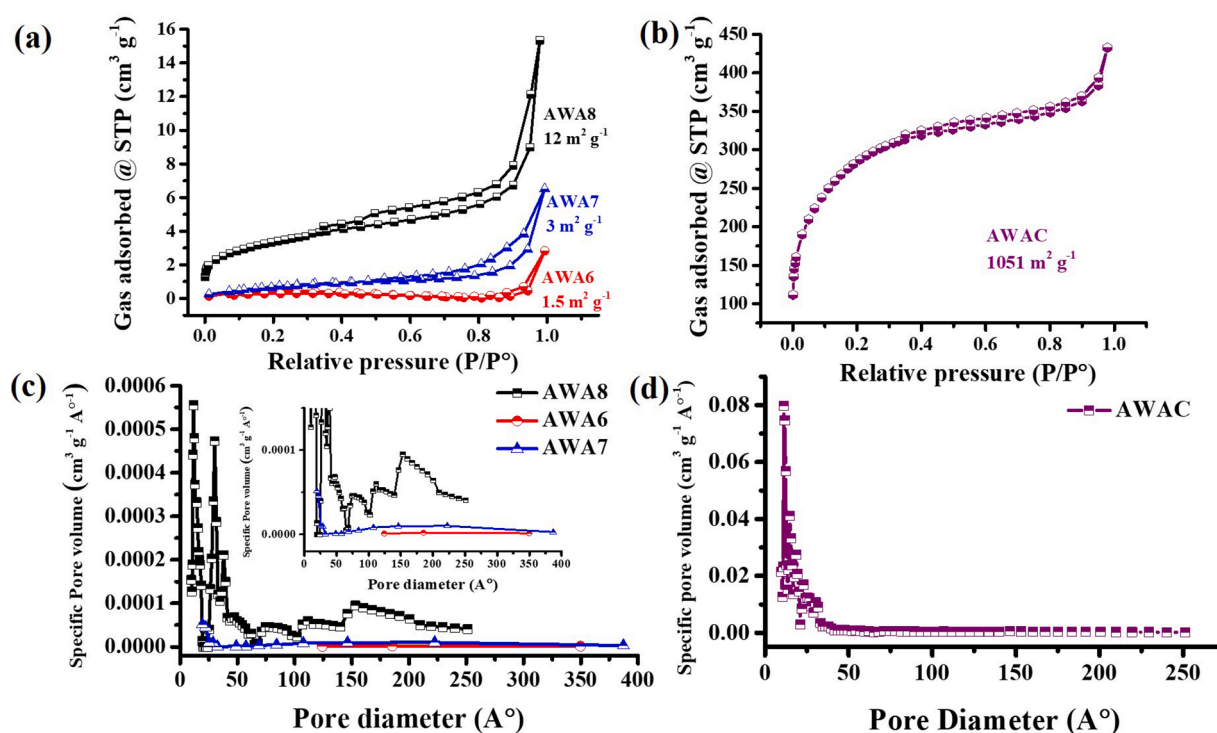

Fig. 4. N$_2$ adsorption studies of (a) AWA6, AWA7, AWA8, and (b) AWAC. BJH pore size distribution of (c) AWA6, AWA7, AWA8, and (d) AWAC.

mesopores of varying sizes are formed, creating the channels for ion passage. While further increasing the temperature to 800 ℃, the creation of micropores <1.5 nm is observed in the distribution plot indicating the rupture of the mesoporous channels and the creation of electrochemically inaccessible and ion-trapping pores. Thus, the mesoporous nature and presence of *in-situ* micro and nano-sized channels in the case of AWA7 is indicative of its better capability of storing Li-ions in a battery-type diffusion mechanism (discussed later).

Electrochemical tests were performed on anode half cells using AWA6, AWA7, and AWA8 electrodes vs. Li/Li$^+$ to understand their compatibility as Li-ion storing battery-type anode and the subsequent achievable storage capacity. The cyclic voltammograms (CVs) of all the anode half cells (Fig. 5a–c) show the characteristic lithiation de-lithiation hysteresis similar to the disordered carbons due to the combined effect of edge or functional group adsorption, intercalation into the interlayer spaces, and micro-/nano-pore filling [12,39,40]. The

majorly irreversible hump at potential above 1.0 V diminishes gradually when the calcination temperature increases from 600- 800 ℃. This may be due to the increase in the ordered nature of the carbon matrix and the subsequent decrease in the trapping of Li-ions in the open carbon edges and functional groups. But the area under the curve, which signifies the quantifiable charge storage (the scan rate being constant), is higher in the case of AWA7 (0.21 W g^{-1}), i.e., when calcined at 700 ℃ compared to 0.18 and 0.16 in case of AWA6 and AWA8 electrodes, respectively. The half-cells were cycled at a low current density of 0.1 A g^{-1}, and the 1st discharge capacity in the case of AWA6, AWA7, and AWA8 electrodes (Fig. 5d–f) were found to be 1041, 1134, and 1059 mAh g^{-1} which decreased to 489, 650, and 493 mAh g^{-1} in the 2nd cycle, respectively. The loss in the capacity after the 1st cycle is due to the formation of the solid electrolyte interface due to the reduction of ethylene carbonate and LiPF$_6$ at the electrode surface and irreversible trapping of ions in the surface functional groups and micro-pores.
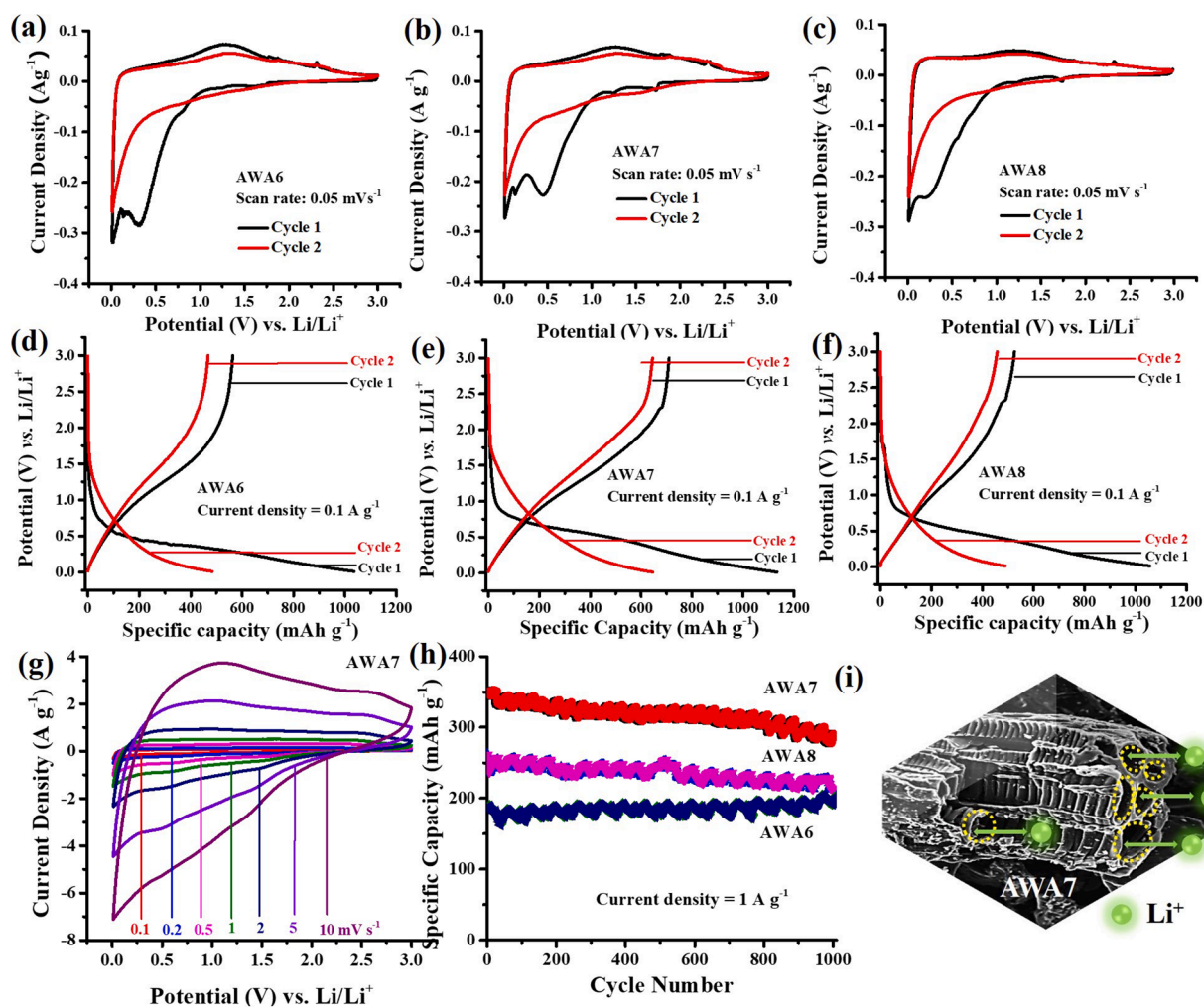
Fig. 5. Cyclic voltammogram of anode half-cell vs. Li/Li$^+$ using (a) AWA6, (b) AWA7, and (c) AWA8 electrodes. Voltage profile of anode half-cell at a low current density of 0.1 A g^{-1} for the (d) AWA6, (e) AWA7, and (f) AWA8 electrodes. (g) CV of AWA7 anode half-cell at different potential scan rates. (h) Cycling stability of AWA6, AWA7, and AWA8 electrodes in half-cell at a current density of 1 A g^{-1}. (i) Schematic of a plausible enhanced Li-ion storage mechanism for AWA7 electrodes.

Further, CVs for AWA7 half-cells were recorded at varying potential sweep rates, which shows the retention of the lithiation-delithiation hysteresis even at a high scan rate of 10 mV s^{-1} (Fig. 5g). When the half-cells were cycled at a high current density of 1 A g^{-1}, AWA7 was found to retain a higher specific capacity of 290 mAh g^{-1} after 1000 cycles compared to 200 and 250 in the case of AWA6, and AWA8, respectively (Fig. 5h). Moreover, when AWA7 was cycled at different current densities from low to high, it was found to deliver a specific capacity of 118 mAh g^{-1} even at a higher current density of 5 A g^{-1} (Supplementary Fig. S2). The better electrochemical performance of AWA7 as anode material for Li-ion storage may be attributed to the micro-sized channels formed in AWA7 (as seen in SEM and TEM images Fig. 3b,f), which leads to more accessible reversible Li-ion storage sites in between the folded carbon sheets. The schematic representation of the plausible Li-ion diffusion and storage mechanism is shown in Fig. 5i.

The activated carbon derived from agro-waste (AWAC) was tested vs. Li/Li$^+$ in the cathodic potential range of 1.5- 4.0 V. The CVs (Fig. 6a) show a near-perfect rectangular I vs. V plot at scan rates of 0.5 to 20 mV s^{-1}, which is the characteristic of EDLC-type ion storage. The deliverable specific capacitances of the AWAC (Fig. 6b–d) in a half-cell configuration were found to be 139.2, 130.3, 120, 118.4, 106.4, 96, and 88 F g^{-1} at current densities of 0.1, 0.2, 0.5, 1, 2, 5, and 10 A g^{-1}, respectively. The AWAC half-cell was found to cycle with ~76% retention till 5000 cycles at a current density of 1 A g^{-1} (Fig. 6e). The initial sharp decrease in capacitance can be due to the presence of ultra-micropores, which can

result in ion-trapping.

On analyzing the individual behavior of the cathode and anode in the half-cell configuration, a LIC full cell was fabricated using a pre-lithiated AWA7 anode and AWAC cathode in a 1:3 mass ratio. The mass ratio was chosen to balance the optimum deliverable energy-power and cycle life. The current realized by an electrode individually in a lithium-ion hybrid capacitor is not the same as that of the current applied. As the cathode-to-anode mass ratio increases, the current realized by the anode increases and vice versa [41,42]. Thus, the diffusion-type charge storage of the battery-type anode decreases. This results in a lower deliverable power density and cycle-life as these are limited by the anode performance, whereas the energy is limited by the cathode. Thus, to balance this performance matrix 1:3 mass ratio is chosen as optimum. The LIC full cell was cycled at different current densities and was found to deliver 84, 66, 60.8, 54.4, and 41 F g^{-1}, at current densities of 0.2, 0.5, 1, 2, and 5 A g^{-1}, respectively with respect to the cathode active mass (Fig. 7a). Moreover, the LIC full cell was found to deliver a specific energy of 120 Wh kg^{-1} at a power density of 434 W kg^{-1}. It could retain 40 Wh kg^{-1} even at a very high-power density of 20.7 kW kg^{-1} which is comparable to or even better than previously reported works of literature (energy and power densities are calculated with respect to the active mass of both the electrodes) (Fig. 7b). The cyclic voltammograms of the LIC full cell at various scan rates were observed to deviate from the rectangular shape obtained in the capacitive cathode half-cell (AWAC vs. Li/Li$^+$, Fig. 6a) due to the contribution from the
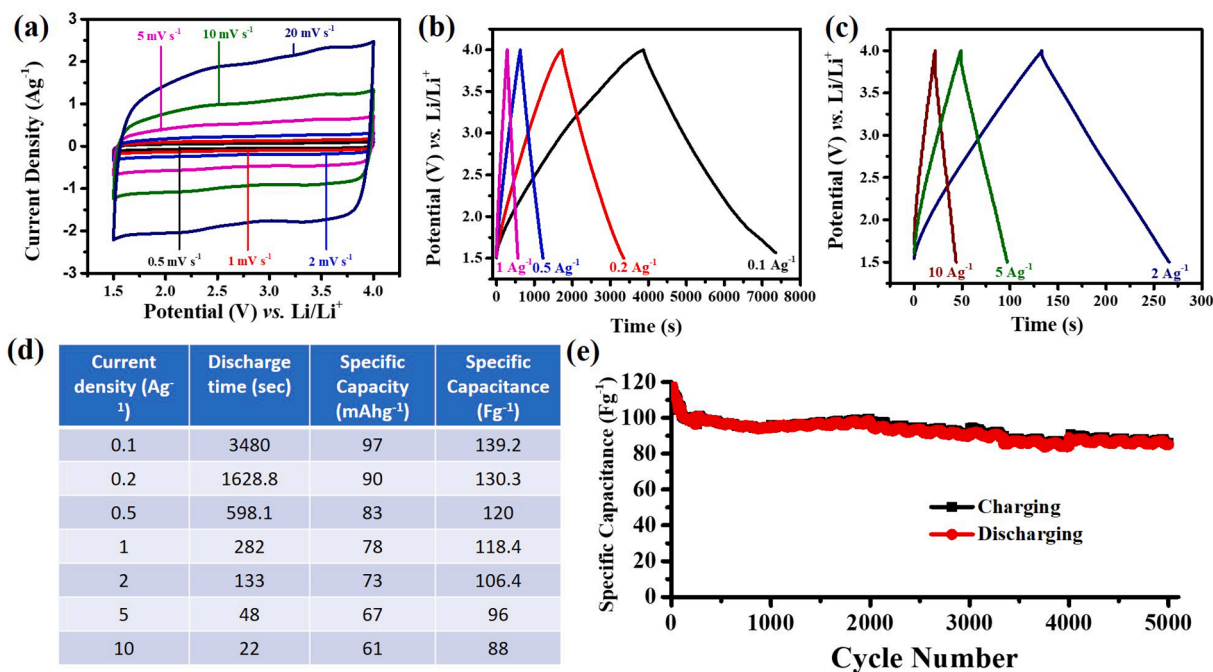
Fig. 6. Electrochemical characterization of AWAC cathode half-cell vs. Li/Li$^+$. (a) CV in the potential ranges between 1.5 and 4.0 V in varying scan rates of 0.5 and 20 mV s^{-1}, (b), (c) Galvanostatic charge-discharge of the half-cell at varying current densities from 0.1- 10 A g^{-1}. (d) Cycling stability of the half-cell at a current density of 1 A g^{-1}.

diffusion-type LIB anode (AWA7) (Fig. 7c). The CVs at varying scan rates were further analyzed using the Cottrell equation, $i = a\nu^b$, and log i vs. log ν plot (Supplementary Fig. S3a). The b-value was evaluated at different potentials. The b-value is 0.5 when the charge storage process is entirely diffusion type and is 1 in the case of capacitive charge storage [34,43]. The b-value lies in the range of 0.5- 1 at all the chosen potentials from the working potential during the charge and discharge scan which signifies the partially capacitive and partially diffusive charge storage behavior of the LIC hybrid full cell (Fig. 7d). The b-value nears 0.5 at potentials below OCV during the discharge scan and high potential near 4 V. The lower b-value at potentials below OCV during the discharge scan may be due to the additional mechanism of pre-lithiated lithium-ion diffusion from the anode in a pre-lithiated LIC. Whereas the lower b-value at potentials near 4 V might be attributed to the anode Li-ion diffusion potential realization at that stage.

In addition to that, the capacitive and diffusive current contribution at different potentials was studied using the equation i(V) = k$_1\nu$ +k$_2\nu^{1/2}$ where k$_1\nu$ is the capacitive and k$_2\nu^{1/2}$ is the diffusive current contribution (Trasatti procedure) [34,43,44]. The i(v)/$\nu^{1/2}$ vs. $\nu^{1/2}$ plot (Supplementary Fig. S3b) was analyzed for k$_1$ and k$_2$ and the partial current contributions. At both potentials below and above OCV (Fig. 7e,f), the capacitive current contribution increases with an increase in potential scan rate due to the faster time scale charge storage. The indications through the b-value in the Cottrell equation are further validated as a higher diffusion-type partial current response is observed at all scan rates for potentials below OCV and high potential around 4 V in the bar graphs (Fig. 7e,f, Supplementary Fig. S3c) as well as the CV separation plot at a current density of 1 A g^{-1} (Fig. 7g). When cycled at a current density of 1 A g^{-1}, the LIC full cell could retain ∼ 67% after 9000 cycles (Fig. 7h).

A series of 3 LED lights were demonstrated using a charged prelithiated AWA7//AWAC full cell (Fig. 8a), and the drop in potential was recorded for 15 min. The intensity of the lights decreases sharply till 1 min, and the multi-colored LEDs emit only low-energy red light after that. The decrease in potential becomes slow after that and feebly lights up till 15 min. The self-discharge for the LIC full cell was studied to understand the shelf-life of the cells, and it could retain ~3.0 V from a

fully charged state till 36 h (Fig. 8b). The higher potential retention may be attributed to the presence of N-doping and functionalities in the AWAC matrix (Figs. 1c, 2g, Supplementary Fig. 1b), which may result in chemisorption and slower loss in the charged state. The leakage current at the highest operational potential hold was found to stabilize in a few minutes and was found to be 1.99 μA at the end of 5 h (Fig. 8c).

The electrochemical impedance spectra for the lithium-ion hybrid capacitor is a result of various contributing factors, including electrolyte solution resistance or ohmic (R$_S$), the charge transfer resistance (C$_T$) (resultant of diffusion-type intercalation (R$_{diff}$), and double layer capacitive adsorption (C$_{dl}$), porous electrode diffusion impedance, Warburg diffusion (Q$_w$) and low-frequency capacitive impedance (C$_w$) [45]. The EIS for the LIC full cell was recorded before and after cycling, and the solution resistance was found to increase from 3.4 to 7.0 Ω.cm^2, whereas the charge transfer resistance was found to increase from 9.8 to 25 Ω.cm^2 (Fig. 8d). The increase in solution transfer resistance may be due to the irreversible consumption of electrolyte ions. On the other hand, the increase in charge transfer resistance may be due to the hindrance and decreases in the charge storage space in the electrode-electrolyte interface and individual electrolytes. Moreover, an increase in the slope of the low-frequency impedance shows a rise in resistance in the diffusion process. Thus, the degradation in performance of the diffusion type LIB anode may be the reason behind the overall degradation in full cell performance.

Dual carbon lithium-ion hybrid capacitors using two mechanistically different disordered carbons are thought to be the optimum hybrid capacitor device because of the comparatively higher reversibility of the LIB-type disordered carbon anodes. Disordered carbon stores Li-ion through various mechanisms including edge adsorption, chemisorption on the heteroatom dopants, intercalation into the interlayer spaces and nano/micro-pore filling. Thus, the ion-storage capacity and efficiency are dependent on the physical and structural characteristics of the carbon, like micro/nano-structures, presence of heteroatoms, and degree of order/disorder. Furthermore, as is observed in the case of AWA7, the micro-channels facilitate more Li-ion storage by providing passage and accessibility to the more electrochemically active sites. In contrast, the activated carbon derived from the same raw material
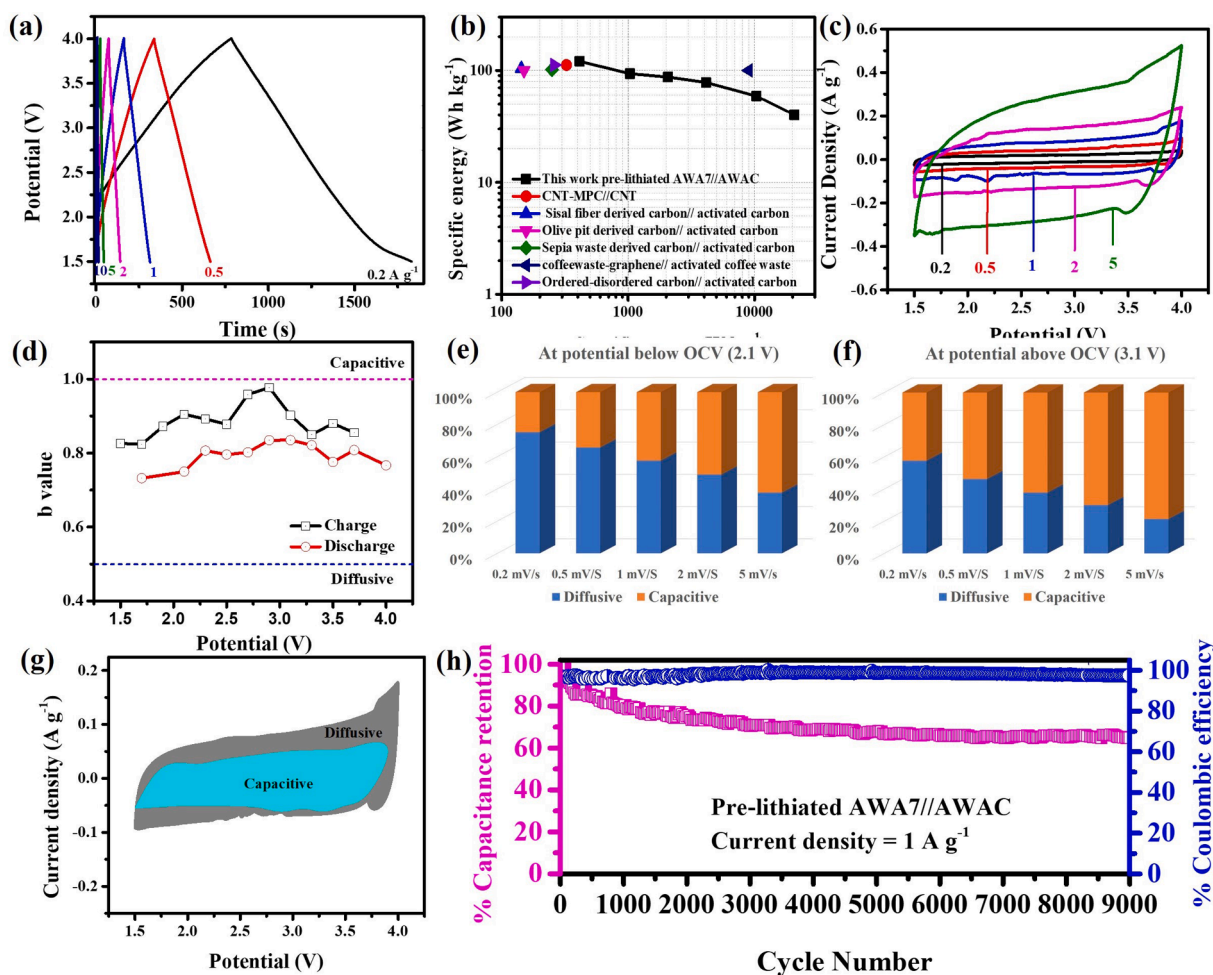
Fig. 7. (a) Galvanostatic charge-discharge profiles of 1:3 pre-lithiated AWA7//AWAC LIC full cell at different current densities (0.2–10 A g^{-1} w.r.t. cathode). (b) Ragone plot of specific power vs. specific energy for the LIC full cell compared to similar reported works of literature. (c) CVs at different potential scan rates (0.5-5.0 mV s^{-1}), (d) The b value vs. potential plot from the Cottrell equation, a bar graph showing the capacitive and diffusive contribution in current response at a different potential, (e) below OCV, and (f) above OCV for the LIC full cell. (g) The separation of capacitive and diffusive current contribution for the CV of the LIC full cell at a scan rate of 1 mV s^{-1}. (h) Cycling stability of the LIC full cell at a current density of 1 A g^{-1} w.r.t. cathode.

served as the capacitive charge storage electrode. Thus, it can be concluded that modifying the same raw material through different pre-treatment strategies and calcination temperatures might result in tuning their physical properties for better electrochemical performance. Thus, dual carbon LICs can be further optimized through tuning the physical properties of the active material, which ultimately translates into their energy storage performances.

4. Conclusions

In this work, a dual carbon lithium-ion capacitor is studied using mechanistically different carbons derived from a single agro-waste precursor as both electrodes. This work emphasizes the role and effect of varying carbon microstructures through the control of synthesis conditions on the Li-ion storage and transport, which consequently translates into the performance of the lithium-ion capacitors. LIB anode-type electrodes were fabricated using hydrothermally treated carbons derived from onion peel agro-waste at different temperatures. When tested in a half cell vs. Li/Li$^+$, the carbon calcined at 700 ℃ delivers optimum performance with a capacity of 290 mAh g^{-1} retained after 1000 cycles at 1 A g^{-1} compared to the carbons calcined at 600 ℃ and 800 ℃. This superiority in performance can be attributed to the micron as well as nano-sized pores or channels formed at 700 ℃, which enables smoother and faster Li-ion passage. In contrast, the activated carbon

derived from onion peel with a blend of micro-, mesoporosity, and surface hetero functionalization was tested as an EDLC-type electrode in a half-cell configuration vs. Li/Li$^+$. This electrode was found to deliver 118 F g^{-1} at 1 A g^{-1}, which was retained 76% after 5000 cycles.

Therefore, a LIC full cell was tested using carbon calcined at 700 ℃ as a anode and activated carbon as a cathode. An optimized mass ratio of 1:3 anode to cathode delivers the energy of 120 Wh kg^{-1} at a power density of 434 W kg^{-1}. The cell was able to retain 40 Wh kg^{-1} even at a higher power density of 20.7 kW kg^{-1}. The LIC full cell could cycle with ~67% capacitance retention till 9000 cycles. The ion-storage mechanism of the LIC full cell was found to more diffusion controlled near the highest operation potential because of the Li-ion diffusion in battery type electrode and, at potentials below OCV because of the parallel pre-lithiated Li-ion diffusion. Further, the capacitive control of the ion-storage was found to increase with higher potential scan rates in CV studies. A set of 3 LEDs connected in series were lit using the fully charged LIC full cell. The cell was found to retain 3.0 V after 36 h when subjected to self-discharge studies, and a leakage current of 1.99 μA was recorded at the end of 5 h. Further, the EIS of the cell recorded after cycling showed an increase in the overall impedance of the system, indicating the degrading state of health of the device with prolonged cycling. Thus, it can be concluded that the ion storage and transport in a dual carbon lithium-ion capacitor system are significantly dependent on the physical and structural properties, and altercations in these
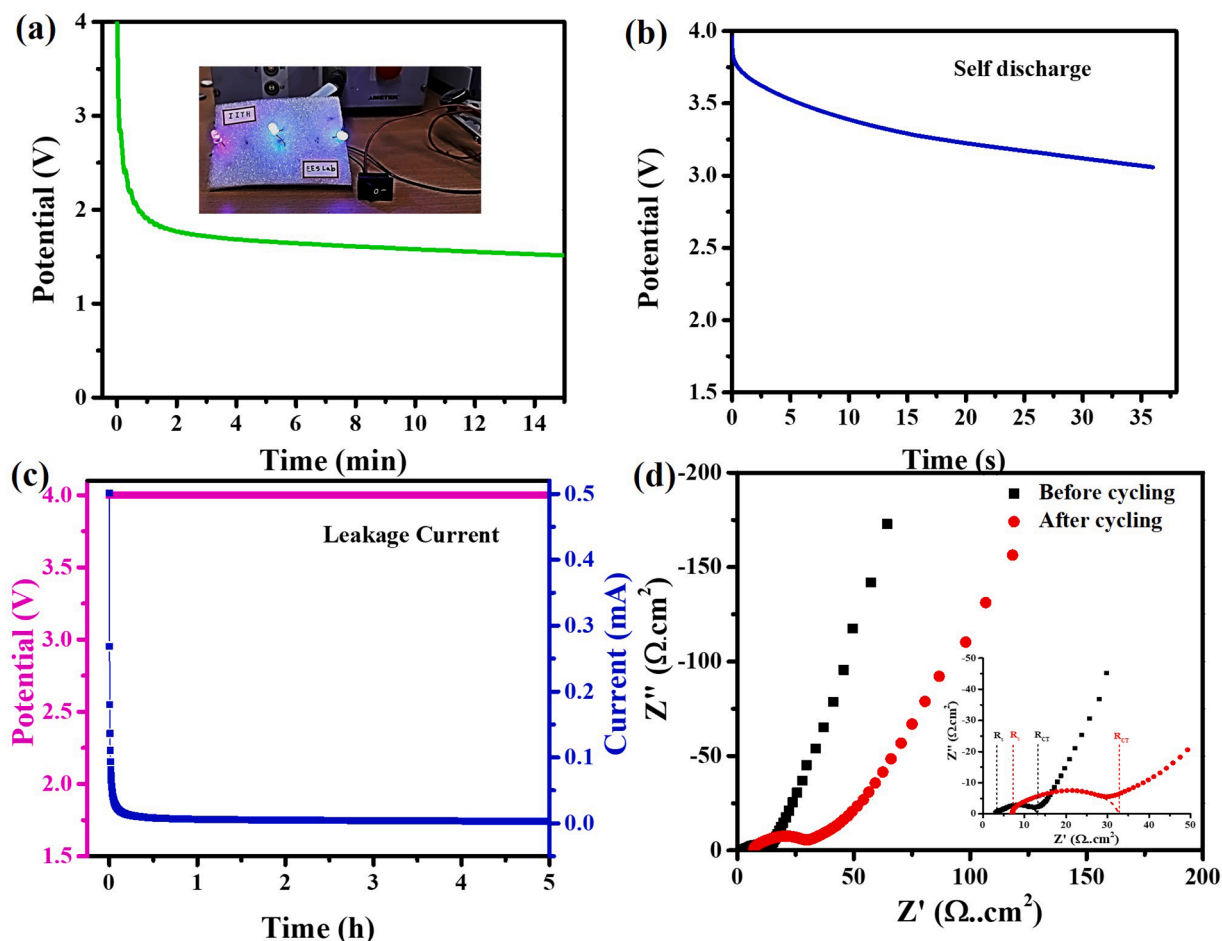
Fig. 8. (a) A series of 3 LED lights demonstration using the pre-lithiated AWA7//AWAC full cell. (b) Self-discharge of the fully charged full cell. (c) Leakage current of the LIC full cell at a voltage hold of 4 V. (d) Electrochemical impedance spectra of the LIC full cell before and after cycling.

properties can result in the optimum deliverable charge storage capacity and consequently energy.

Declaration of Competing Interest

The authors declare that they have no known competing financial interests or personal relationships that could have appeared to influence the work reported in this paper.

Data availability

The data that has been used is confidential.

Acknowledgments

Supplementary materials

Supplementary material associated with this article can be found, in the online version, at doi:10.1016/j.electacta.2023.142353.

References

[1] J. Ding, W. Hu, E. Paek, D. Mitlin, Review of hybrid ion capacitors: from aqueous to lithium to sodium, Chem. Rev. 118 (2018) 6457–6498, https://doi.org/10.1021/acs.chemrev.8b00116.

[2] C. Han, H. Li, R. Shi, L. Xu, J. Li, F. Kang, B. Li, Nanostructured anode materials for non-aqueous lithium ion hybrid capacitors, Energy Environ. Mater. 1 (2018) 75–87, https://doi.org/10.1002/eem2.12009.

[3] B. Li, J. Zheng, H. Zhang, L. Jin, D. Yang, H. Lv, C. Shen, A. Shellikeri, Y. Zheng, R. Gong, Electrode materials, electrolytes, and challenges in nonaqueous lithium-ion capacitors, Adv. Mater. 30 (2018), 1705670, https://doi.org/10.1002/adma.201705670.

[4] L. Xia, B. Tang, J. Wei, Z. Zhou, Recent advances in alkali metal-ion hybrid supercapacitors, Batter. Supercaps 4 (2021) 1108–1121, https://doi.org/10.1002/batt.202000332.

[5] J.M. Campillo-Robles, X. Artetxe, K. del Teso Sánchez, C. Gutiérrez, H. Macicior, S. Röser, R. Wagner, M. Winter, General hybrid asymmetric capacitor model: validation with a commercial lithium ion capacitor, J. Power Sources 425 (2019) 110–120, https://doi.org/10.1016/j.jpowsour.2019.03.121.

[6] G.G. Amatucci, F. Badway, A. Du Pasquier, T. Zheng, An asymmetric hybrid nonaqueous energy storage cell, J. Electrochem. Soc. 148 (2001) A930, https://doi.org/10.1149/1.1383553.

[7] W. Liu, X. Zhang, Y. Xu, C. Li, K. Wang, X. Sun, F. Su, C.M. Chen, F. Liu, Z.S. Wu, Y. Ma, Recent advances on carbon-based materials for high performance lithium-ion capacitors, Batter. Supercaps 4 (2021) 407–428, https://doi.org/10.1002/batt.202000264.

[8] L. Jin, C. Shen, A. Shellikeri, Q. Wu, J. Zheng, P. Andrei, J.G. Zhang, J.P. Zheng, Progress and perspectives on pre-lithiation technologies for lithium ion capacitors, Energy Environ. Sci. 13 (2020) 2341–2362, https://doi.org/10.1039/D0EE00807A.

[9] J.P. Zheng, High energy density electrochemical capacitors without consumption of electrolyte, J. Electrochem. Soc. 156 (2009) A500, https://doi.org/10.1149/1.3121564.

[10] M. Arnaiz, J. Ajuria, Pre-lithiation strategies for lithium ion capacitors: past, present, and future, Batter. Supercaps 4 (2021) 733–748, https://doi.org/10.1002/batt.202000328.

[11] X. Dou, I. Hasa, D. Saurel, C. Vaalma, L. Wu, D. Buchholz, D. Bresser, S. Komaba, S. Passerini, Hard carbons for sodium-ion batteries: structure, analysis, sustainability, and electrochemistry, Mater. Today 23 (2019) 87–104, https://doi.org/10.1016/j.mattod.2018.12.040.

[12] D.A. Stevens, J.R. Dahn, The mechanisms of lithium and sodium insertion in carbon materials, J. Electrochem. Soc. 148 (2001) A803, https://doi.org/10.1149/1.1379565.

[13] Y. Gao, Z. Yang, Y. Wang, X. Wang, Boosting capacitive storage of cathode for lithium-ion capacitors: combining pore structure with P-doping, Electrochim. Acta 368 (2021), 137646, https://doi.org/10.1016/j.electacta.2020.137646.

[14] W. Chen, M. Gong, K. Li, M. Xia, Z. Chen, H. Xiao, Y. Fang, Y. Chen, H. Yang, H. Chen, Insight into KOH activation mechanism during biomass pyrolysis: chemical reactions between O-containing groups and KOH, Appl. Energy 278 (2020), 115730, https://doi.org/10.1016/j.apenergy.2020.115730.

[15] T.S. Hui, M.A.A. Zaini, Potassium hydroxide activation of activated carbon: a commentary, Carbon Lett. 16 (2015) 275–280, https://doi.org/10.5714/CL.2015.16.4.275.

[16] X. Dai, S. Lei, J. Liu, Z. Shang, S. Zhong, X. Li, Promoting the energy density of lithium-ion capacitor by coupling the pore-size and nitrogen content in capacitive carbon cathode, J. Power Sources 498 (2021), 229912, https://doi.org/10.1016/j.jpowsour.2021.229912.

[17] L. Li, D. Zhang, J. Deng, Y. Gou, J. Fang, H. Cui, Y. Zhao, M. Cao, Carbon-based materials for fast charging lithium-ion batteries, Carbon 183 (2021) 721–734, https://doi.org/10.1016/j.carbon.2021.07.053.

[18] P. Dubey, V. Shrivastav, P.H. Maheshwari, S. Sundriyal, Recent advances in biomass derived activated carbon electrodes for hybrid electrochemical capacitor applications: challenges and opportunities, Carbon 170 (2020) 1–29, https://doi.org/10.1016/j.carbon.2020.07.056.

[19] E. Frackowiak, F. Béguin, Carbon materials for the electrochemical storage of energy in capacitors, Carbon 39 (2001) 937–950, https://doi.org/10.1016/S0008-6223(00)00183-4.

[20] S.S. Zhang, Dual-carbon lithium-ion capacitors: principle, materials, and technologies, Batter. Supercaps 3 (2020) 1137–1146, https://doi.org/10.1002/batt.202000133.

[21] P. Sennu, N. Arun, S. Madhavi, V. Aravindan, Y.S. Lee, All carbon based high energy lithium-ion capacitors from biomass: the role of crystallinity, J. Power Sources 414 (2019) 96–102, https://doi.org/10.1016/j.jpowsour.2018.12.089.

[22] M. Schroeder, S. Menne, J. Ségalini, D. Saurel, M. Casas-Cabanas, S. Passerini, M. Winter, A. Balducci, Considerations about the influence of the structural and electrochemical properties of carbonaceous materials on the behavior of lithium-ion capacitors, J. Power Sources 266 (2014) 250–258, https://doi.org/10.1016/j.jpowsour.2014.05.024.

[23] S. Kumagai, Y. Abe, T. Saito, T. Eguchi, M. Tomioka, M. Kabir, D. Tashima, Lithium-ion capacitor using rice husk-derived cathode and anode active materials adapted to uncontrolled full-pre-lithiation, J. Power Sources 437 (2019) 226924, https://doi.org/10.1016/j.jpowsour.2019.226924.

[24] J. Ajuria, E. Redondo, M. Arnaiz, R. Mysyk, T. Rojo, E. Goikolea, Lithium and sodium ion capacitors with high energy and power densities based on carbons from recycled olive pits, J. Power Sources 359 (2017) 17–26, https://doi.org/10.1016/j.jpowsour.2017.04.107.

[25] Z. Yang, H. Guo, X. Li, Z. Wang, Z. Yan, Y. Wang, Natural sisal fibers derived hierarchical porous activated carbon as capacitive material in lithium ion capacitor, J. Power Sources 329 (2016) 339–346, https://doi.org/10.1016/j.jpowsour.2016.08.088.

[26] J. Jiang, Y. Zhang, Z. Li, Y. An, Q. Zhu, Y. Xu, S. Zang, H. Dou, X. Zhang, Defect-rich and N-doped hard carbon as a sustainable anode for high-energy lithium-ion capacitors, J. Colloid Interface Sci. 567 (2020) 75–83, https://doi.org/10.1016/j.jcis.2020.01.120.

[27] J.L. Gómez-Urbano, G. Moreno-Fernández, M. Arnaiz, J. Ajuria, T. Rojo, D. Carriazo, Graphene-coffee waste derived carbon composites as electrodes for optimized lithium ion capacitors, Carbon 162 (2020) 273–282, https://doi.org/10.1016/j.carbon.2020.02.052.

[28] W. Zhao, J. Yang, Y. Shang, B. Yang, D. Han, G. Du, Q. Su, S. Ding, B. Xu, A. Cao, 3D carbon nanotube-mesoporous carbon sponge with short pore channels for high-power lithium-ion capacitor cathodes, Carbon 203 (2023) 479–489, https://doi.org/10.1016/j.carbon.2022.12.009.

[29] J. Sun, G. Li, Z. Wang, H. Guo, X. Li, G. Yan, J. Wang, Balancing the anions adsorption and intercalation in carbon cathode enables high energy density dual-carbon lithium-ion capacitors, Carbon 200 (2022) 28–37, https://doi.org/10.1016/j.carbon.2022.08.046.

[30] T. Qian, Y. Huang, M. Zhang, Z. Xia, H. Liu, L. Guan, H. Hu, M. Wu, Non-corrosive and low-cost synthesis of hierarchically porous carbon frameworks for high-performance lithium-ion capacitors, Carbon 173 (2021) 646–654, https://doi.org/10.1016/j.carbon.2020.11.051.

[31] B. Li, H. Zhang, D. Wang, H. Lv, C. Zhang, Agricultural waste-derived activated carbon for high performance lithium-ion capacitors, RSC Adv. 7 (2017) 37923–37928, https://doi.org/10.1039/C7RA06680E.

[32] A. Gopalakrishnan, S. Badhulika, From onion skin waste to multi-heteroatom self-doped highly wrinkled porous carbon nanosheets for high-performance supercapacitor device, J. Energy Storage 38 (2021), 102533, https://doi.org/10.1016/j.est.2021.102533.

[33] M.D. Mehare, A.D. Deshmukh, S.J. Dhoble, Preparation of porous agro-waste-derived carbon from onion peel for supercapacitor application, J. Mater. Sci. 55 (2020) 4213–4224, https://doi.org/10.1007/s10853-019-04236-7.

[34] U. Bhattacharjee, S. Bhowmik, S. Ghosh, N. Vangapally, S.K. Martha, Boron-doped graphene anode coupled with microporous activated carbon cathode for lithium-ion ultracapacitors, Chem. Eng. J. 430 (2022), 132835, https://doi.org/10.1016/j.cej.2021.132835.

[35] P.M. Chu, F.R. Guenther, G.C. Rhoderick, W.J. Lafferty, The NIST quantitative infrared database, J. Res. Natl. Inst. Stand. Technol. 104 (1999) 59, https://doi.org/10.6028/jres.104.004.

[36] J.R. Rumble Jr, D.M. Bickham, C.J. Powell, The NIST x-ray photoelectron spectroscopy database, Surf. Interface Anal. 19 (1992) 241–246, https://doi.org/10.1002/sia.740190147.

[37] S.S. Kim, L. Britcher, S. Kumar, H.J. Griesser, XPS study of sulfur and phosphorus compounds with different oxidation states, JSM 47 (2018) 1913–1922, https://doi.org/10.17576/jsm-2018-4708-33.

[38] M. Thommes, K. Kaneko, A.V. Neimark, J.P. Olivier, F. Rodriguez-Reinoso, J. Rouquerol, K.S. Sing, Physisorption of gases, with special reference to the evaluation of surface area and pore size distribution (IUPAC Technical Report), Pure Appl. Chem. 87 (2015) 1051–1069, https://doi.org/10.1515/pac-2014-1117.

[39] X. Dou, I. Hasa, D. Saurel, C. Vaalma, L. Wu, D. Buchholz, D. Bresser, S. Komaba, S. Passerini, Hard carbons for sodium-ion batteries: structure, analysis, sustainability, and electrochemistry, Mater. Today 23 (2019) 87–104, https://doi.org/10.1016/j.mattod.2018.12.040.

[40] R. Mukherjee, A.V. Thomas, D. Datta, E. Singh, J. Li, O. Eksik, V.B. Shenoy, N. Koratkar, Defect-induced plating of lithium metal within porous graphene networks, Nat. Commun. 5 (2014) 1–10, https://doi.org/10.1038/ncomms4710.

[41] V. Surendran, A. Lal, M.M. Shaijumon, Mass balancing of hybrid ion capacitor electrodes: a simple and generalized semiempirical approach, ACS Appl. Mater. Interfaces 13 (2021) 52610–52619, https://doi.org/10.1021/acsami.1c14731.

[42] L. Jin, X. Guo, C. Shen, N. Qin, J. Zheng, Q. Wu, C. Zhang, J.P. Zheng, A universal matching approach for high power-density and high cycling-stability lithium ion capacitor, J. Power Sources 441 (2019), 227211, https://doi.org/10.1016/j.jpowsour.2019.227211.

[43] U. Bhattacharjee, S. Bhowmik, S. Ghosh, S.K. Martha, Effect of *in-situ* derived sulfur dispersion on dual carbon lithium-ion capacitors, J. Power Sources 542 (2022), 231768, https://doi.org/10.1016/j.jpowsour.2022.231768.

[44] S. Ardizzone, G. Fregonara, S. Trasatti, "Inner" and "outer" active surface of RuO_2 electrodes, Electrochim. Acta 35 (1990) 263–267, https://doi.org/10.1016/0013-4686(90)85068-X.

[45] X. Zhang, X. Zhang, X. Sun, Y. An, S. Song, C. Li, K. Wang, F. Su, C.M. Chen, F. Liu, Electrochemical impedance spectroscopy study of lithium-ion capacitors: modeling and capacity fading mechanism, J. Power Sources 488 (2021), 229454, https://doi.org/10.1016/j.jpowsour.2021.229454.